ROYAL SOCIETY OPEN SCIENCE

royalsocietypublishing.org/journal/rsos

Research

Cite this article: Lu D, Yang F, Dun C, Guo J, Urban JJ, Belova L. 2024 Inkjet-printed SnO_x as an effective electron transport layer for planar perovskite solar cells and the effect of Cu doping. *R. Soc. Open Sci.* **11**: 231331.
https://doi.org/10.1098/rsos.231331

Received: 7 September 2023
Accepted: 22 January 2024

Subject Category:
Engineering

Subject Areas:
materials science/chemical engineering/nanotechnology

Keywords:
inkjet printing, SnO_x, Cu doping, perovskite solar cells, hysteresis, low-temperature solution process

Author for correspondence:
Liubov Belova
e-mail: lyuba@kth.se

†Present address: National Synchrotron Light Source II, Brookhaven National Laboratory, Upton, NY 11973, USA.

Electronic supplementary material is available online at https://doi.org/10.6084/m9.figshare.c.7074851.

THE ROYAL SOCIETY PUBLISHING

Inkjet-printed SnO_x as an effective electron transport layer for planar perovskite solar cells and the effect of Cu doping

Dongli Lu[1], Feipeng Yang[2,†], Chaochao Dun[3], Jinghua Guo[2], Jeffrey J. Urban[3] and Liubov Belova[1]

[1]Department of Materials Science and Engineering, KTH Royal Institute of Technology, Stockholm 10044, Sweden
[2]Joint Center for Energy Storage Research, and [3]The Molecular Foundry, Lawrence Berkeley National Laboratory, Berkeley, CA 94720, USA

DL, 0000-0002-8202-6233; FY, 0000-0002-5470-3241

Inkjet printing is a more sustainable and scalable fabrication method than spin coating for producing perovskite solar cells (PSCs). Although spin-coated SnO_2 has been intensively studied as an effective electron transport layer (ETL) for PSCs, inkjet-printed SnO_2 ETLs have not been widely reported. Here, we fabricated inkjet-printed, solution-processed SnO_x ETLs for planar PSCs. A champion efficiency of 17.55% was achieved for the cell using a low-temperature processed SnO_x ETL. The low-temperature SnO_x exhibited an amorphous structure and outperformed high-temperature crystalline SnO_2. The improved performance was attributed to enhanced charge extraction and transport and suppressed charge recombination at ETL/perovskite interfaces, which originated from enhanced electrical and optical properties of SnO_x, improved perovskite film quality, and well-matched energy level alignment between the SnO_x ETL and the perovskite layer. Furthermore, SnO_x was doped with Cu. Cu doping increased surface oxygen defects and upshifted energy levels of SnO_x, leading to reduced device performance. A tunable hysteresis was observed for PSCs with Cu-doped SnO_x ETLs, decreasing at first and turning into inverted hysteresis afterwards with increasing Cu doping level. This tunable hysteresis was related to the interplay between charge/ion accumulation and recombination at ETL/perovskite interfaces in the case of electron extraction barriers.

1. Introduction

Perovskite solar cells (PSCs) have achieved a power conversion efficiency (PCE) reaching 26% after a fast development during the past decade [1]. However, there is still a lack of a reliable large-scale manufacturing method that can reduce the production cost of PSCs and simultaneously offer PSC device performance comparable to that of conventional spin coating. Inkjet printing is considered as an alternative deposition method to spin coating because of its potential for large-scale manufacturing [2]. Moreover, its drop-on-demand technology produces almost no material waste. In recent years, partially inkjet-printed PSCs have been demonstrated [3–5] while inkjet-printed SnO_2 electron transport layers (ETLs) have not been widely reported. Rohnacher *et al*. fabricated SnO_x ETLs using inkjet printing and achieved a PCE of 18.8% with severe hysteresis [6]. Ghahremani *et al*. reported an optimal PCE of 13.08% for devices using inkjet-printed SnO_2 ETLs [7]. In our previous work, we achieved a PCE of 17.37% for inkjet-printed SnO_2 ETLs prepared from a commercial colloidal SnO_2 dispersion [8]. More studies with detailed analysis are required to move closer to large-scale device applications.

As a key component of PSCs, ETLs play an important role in transporting electrons and blocking holes [9]. For a long time, TiO_2 has served as the most widely used electron transport material because of its abundance and favourable energy band alignment with perovskites [10]. However, TiO_2 has its own limitations. For example, its photoactivity deteriorates device stability under ultraviolet (UV) illumination; a high sintering temperature (greater than 450°C) is required for proper crystallinity of TiO_2, which is not compatible with flexible PSCs [11,12]. Thereafter, SnO_2 has attracted considerable attention because of its potential to overcome the disadvantages of TiO_2. SnO_2 has a slightly wider band gap (above 3.6 eV) than TiO_2, allowing for a longer device stability upon exposure to UV light [13]. It also has an electron mobility of up to 240 $cm^2\ V^{-1}\ s^{-1}$, which is 100 times higher than that of TiO_2 [12]. Regarding the fabrication of SnO_2 ETLs, a high-temperature sintering process is not a must. Low-temperature processed SnO_2 ETLs have been reported to deliver high device performance [14–16], even superior to that of their high-temperature processed counterparts [17,18]. Up to now, the main strategy for boosting the performance and stability of SnO_2 based devices has been to suppress energy loss within SnO_2 [19,20] or at the ETL/perovskite interface [21–23]. Doping is a direct and effective method of modifying the properties of SnO_2, such as the conductivity and work function, which can facilitate electron extraction and transport [24]. It is also easily compatible with a solution process. For the selection of doping elements, a broad range of dopants has been tested, such as Li [25], Ga [26], Nb [27], Zn [28] and Sb [29]. To the best of our knowledge, there are only two reports in which Cu-doped SnO_2 was used as an ETL for PSCs. Zhou *et al*. applied Cu-doped SnO_2 ETLs in planar PSCs and achieved an enhanced PCE of 21% (19.63% for undoped SnO_2-based PSCs) and improved long-term stability [30]. In the other study [31], based on a low-temperature solution-processed Cu-doped SnO_2 ETL, the PSC device exhibited a PCE of 11.29% and a fill factor (FF) of 73.38% compared to the undoped device with a PCE of 8.32% and an FF of 59.9%. Therefore, there is a need for more comprehensive studies on the effects of Cu doping on device performance to unveil the underlying mechanisms.

In this study, we conducted a systematic investigation of the application of inkjet-printed solution-processed SnO_x ETLs in planar PSCs. The effect of the annealing temperature of SnO_x ETLs was studied, and low-temperature amorphous SnO_x outperformed high-temperature crystalline SnO_2. The amorphous SnO_x enabled the formation of high-quality perovskite films. SnO_x also exhibited improved electrical and optical properties and better energy level alignment with the perovskite layer, facilitating charge transport and reducing charge recombination at ETL/perovskite interfaces. An optimum PCE of 17.55% was achieved for planar PSCs using inkjet-printed amorphous SnO_x ETLs. Afterwards, Cu was incorporated into SnO_x. Upon Cu doping, SnO_x exhibited increased surface defects and upshifted energy levels, and the perovskite film exhibited increased defects, resulting in reduced device performance. A tunable hysteresis was observed for PSCs based on Cu-doped SnO_x ETLs with variations in the Cu doping level, originating from the interaction of ion/charge accumulation and recombination at ETL/perovskite interfaces in the case of extraction barriers.

2. Material and methods

2.1. Materials

All chemicals were purchased off the shelf and were used without further modifications. Tin(IV) acetate ($Sn(CH_3CO_2)_4$) and copper(II) acetate ($Cu(CO_2CH_3)_2$, 99.99%) were purchased from Sigma–Aldrich

(Darmstadt, Germany). Lead iodide (PbI_2, 99.99%) and lead bromide ($PbBr_2$, >98.0%) were purchased from TCI (Tokyo, Japan). Formamidinium iodide (FAI, $CH(NH_2)_2I$, >98%) and methylammonium bromide (MABr, CH_3NH_3Br, >98%) were purchased from Dyenamo (Stockholm, Sweden) and Sigma–Aldrich (Darmstadt, Germany), respectively. Spiro-OMeTAD (99.8%) was purchased from Borun New Material Technology (Ningbo, China). Bis(trifluoromethane)sulfonimide lithium salt (LiTFSI, 99.95%), FK 209 Co(III) TFSI salt (FK 209, 98%), and 4-*tert*-butylpyridine (TBP, 98%) were purchased from Sigma–Aldrich (Darmstadt, Germany).

2.2. Inkjet printing of pristine and Cu-doped SnO_x thin layers

A customized drop-on-demand inkjet printing system was used in our laboratory, which was designed for the piezoelectric-driven printheads from XaarJet [32]. The inkjet printing of SnO_x and Cu-doped SnO_x was performed under ambient conditions using XJ126/80 printheads with 126 active nozzles and a drop volume of 80 pL. More technical information on the printheads is presented in electronic supplementary material, table S1. A customized waveform was used with a peak voltage of 20 V and a jetting pulse of 20 µs. The printing frequency was set as 283.46 Hz and the printing resolution was 360 dpi.

SnO_x thin films were inkjet-printed using inks with tin(IV) acetate dissolved in a solution consisting of 2-propanol and propylene glycol (9/1, v/v). A few drops of ethanolamine were added to improve solubility of tin acetate. For printing, a substrate was placed on a pre-heated printing stage at 60°C; 5 min after printing, the substrate was transferred to a furnace and annealed at 220°C for 1 h. Cu-doped SnO_x was fabricated using a process similar to that of pristine SnO_x. A certain amount of Cu acetate solution, containing 0.25 M Cu acetate dissolved in a mixed solvent of 2-propanol and propylene glycol (9/1, v/v), was added to the Sn acetate solution. The amount of the added Cu acetate solution was determined based on the desired doping level. The mixed solution was then printed, and the resulting film was annealed at 220°C for 1 h.

2.3. Device fabrication

Fluorine-doped tin oxide (FTO) glass substrates (14 $\Omega\,sq^{-1}$, Pilkington TEC) were cut into pieces with dimensions of 25 mm × 15 mm. Each piece was etched at the edge with Zn powder and 2 M HCl aqueous solution. After that, the substrates were sonicated in the sequence of 5% deconex water solution, deionized water, acetone, and 2-propanol for 15 min. Before inkjet printing of the ETL, the FTO substrate was pre-heated at 500°C for 30 min (pre-heating treatment) and afterwards cooled down to room temperature. A compact SnO_x or Cu-doped SnO_x ETL was fabricated as described above. For fabrication of the perovskite layer, we followed the procedure reported in [8,33]. To prepare the perovskite precursor, 1.1 M PbI_2, 1 M FAI, 0.2 M $PbBr_2$ and 0.2 M MABr were dissolved in a mixed solvent (*N*,*N*-dimethylformamide/dimethyl sulfoxide, 4/1 v/v). From that volume, 75 µl of the perovskite precursor was spin-coated at 4500 rpm for 30 s, and meanwhile 125 µl of chlorobenzene was dripped onto the perovskite film 15 s before the end of spin coating. The resulting perovskite film was immediately transferred to a hotplate and dried at 100°C for 30 min. A hole transport layer was prepared by spin-coating at 4000 rpm for 30 s using a precursor containing 70 mM Spiro-OMeTAD, 20 mM LiTFSI, 200 mM TBP, and 2 mM FK 209 in chlorobenzene. Finally, an Au electrode with a thickness of 80 nm was deposited via thermal evaporation (Edwards Auto 306).

2.4. Characterization

The surface morphology and cross-sectional microstructure were analysed via a combined focused ion beam/scanning electron microscope (FIB/SEM, FEI Nova 600 Nanolab, ThermoFisher, Eindhoven, Netherlands). The X-ray diffraction (XRD) analysis was performed using an X-ray diffractometer (Siemens D5000, Siemens, Munich, Germany) with the use of Cu Kα1 radiation ($\lambda = 1.5406$ Å). The characterized areas of the solar cells were defined by masks of 0.126 cm^2 and illuminated under an AM 1.5G solar simulator (Newport 91160–1000) with an incident light density of 100 $mW\,cm^{-2}$. Photocurrent density–voltage (J–V) data were collected by a Keithley 2400 unit with a scan rate of 125 $mV\,s^{-1}$. X-ray photoelectron spectroscopy (XPS) and ultraviolet photoelectron spectroscopy (UPS) measurements were conducted using a K-Alpha XPS/UPS system manufactured by Thermo Scientific. For XPS analysis, the spectra were obtained using a monochromatized Al Kα line with a photon energy ($h\nu$) of 1486.6 eV. For UPS analysis, a He1 ultraviolet light source with an energy of 21.22 eV was employed. The valence band photoelectron signal originated from the top 2–3 nm of the sample surface,

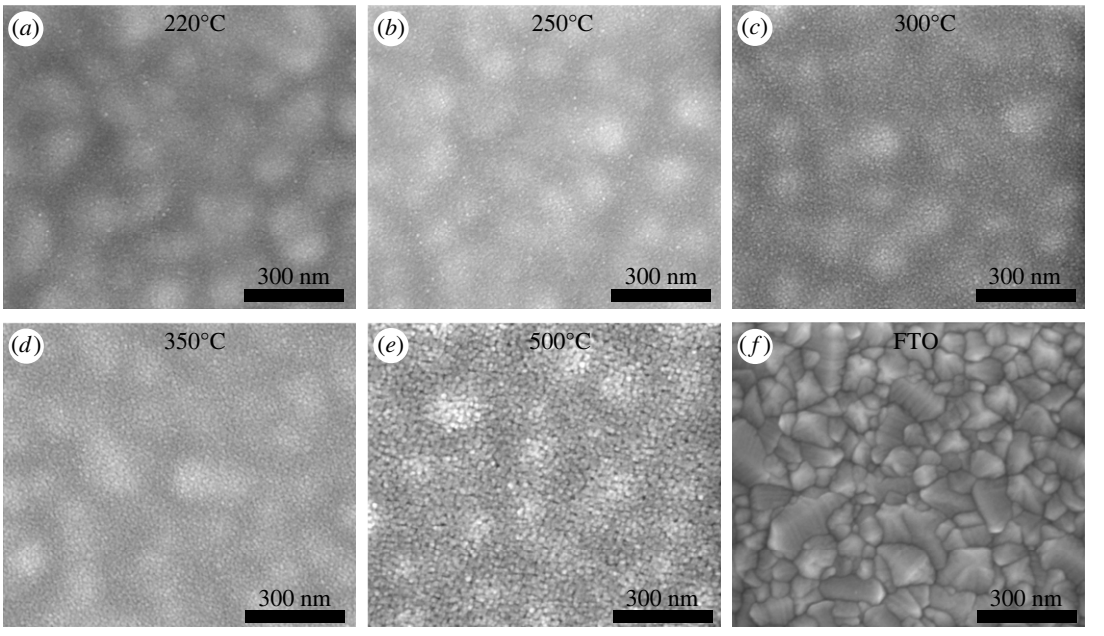

Figure 1. Top-view SEM images of inkjet-printed SnO_x thin films annealed at various temperatures: (*a*) 220°C, (*b*) 250°C, (*c*) 300°C, (*d*) 350°C, and (*e*) 500°C. A bare FTO substrate is shown in (*f*). Note that larger spherical features in (*a–e*) are from the FTO beneath the SnO_x films, which has a substantially higher roughness (*f*).

and the electronic work function of the material surface was measured. Sn $M_{5,4}$-edge and O K-edge X-ray absorption spectroscopy (XAS) measurements were conducted on BL7.3.1 and 8.0.1.4 at the Advanced Light Source (ALS). The ultraviolet–visible (UV/Vis) absorption and transmission spectra were obtained using a Lambda 750 spectrophotometer. The conductivity of the ETLs was measured using a two-probe method [33], and the current–voltage (I–V) characteristics were collected by a Keithley 2400 unit. The steady-state photoluminescence (PL) of the perovskite films was investigated using a CARY Eclipse fluorescence spectrophotometer with an excitation wavelength of 450 nm.

3. Results and discussion

3.1. Inkjet-printed solution-processed SnO_x electron transport layer

In this work, we prepared SnO_x thin films using precursor inks consisting of tin(IV) acetate. The drying mechanism of these inkjet-printed thin films is different from that of their spin-coated counterparts prepared from $SnCl_2$ or tin(IV) isopropoxide precursors [17,18]. Therefore, the effect of the annealing temperature was studied to find the optimal annealing temperature for SnO_x ETLs. A schematic diagram of the inkjet-printed solution-processed SnO_x is shown in electronic supplementary material, figure S1. Figure 1 shows top-view SEM images of the printed films annealed at various temperatures. All the printed films were uniform and continuous, with no pinholes observed. Obvious granular features appeared at 300°C. The particles became larger and the films exhibited more porosity when the temperature was further increased to 500°C. This was confirmed by the XRD patterns displayed in figure 2*a*. The printed SnO_x thin films annealed below 300°C exhibited an amorphous phase with no diffraction peaks detected. The characteristic peaks attributed to tetragonal rutile crystalline phases of SnO_2 (JCPDS 41-1445) were observed at and above 300°C [17,34]. The intensities of these peaks increased with increasing annealing temperature.

Planar PSCs (figure 2*b*) were then fabricated using inkjet-printed SnO_x ETLs annealed at various temperatures ranging from 210°C to 500°C. The J–V curves of the devices are shown in figure 2*c*. The photovoltaic parameters and their statistical distributions are presented in detail in electronic supplementary material, table S2 and figure S2, respectively. The cells based on 220°C-annealed SnO_x ETLs achieved the highest PCE of 15.70% (table 1). When the annealing temperature decreased from 220°C to 200°C, the short-circuit current density (J_{SC}) and FF both decreased dramatically, and J_{SC} almost dropped to 0 at 200°C. The reason could be that tin acetate did not decompose completely at

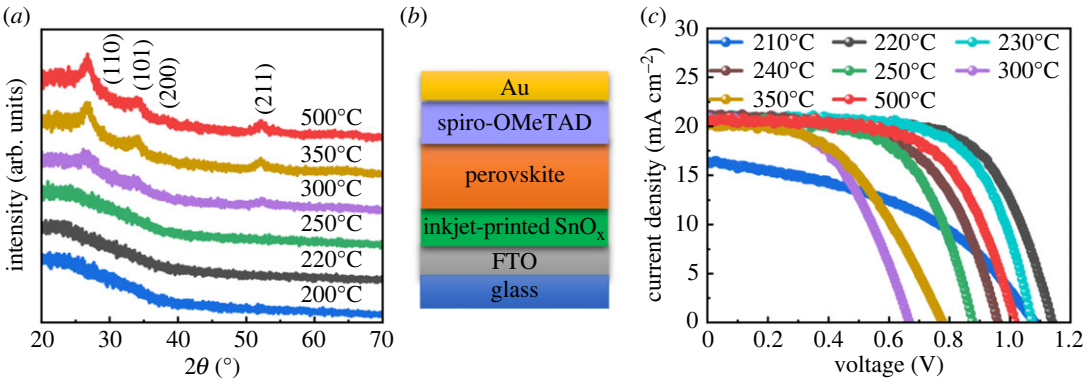

Figure 2. (*a*) Temperature-dependent XRD patterns of SnO_x thin films inkjet-printed on glass substrates; (*b*) device configuration and (*c*) J–V curves of PSCs based on inkjet-printed SnO_x ETLs annealed at various temperatures.

Table 1. Photovoltaic parameters of PSCs with inkjet-printed SnO_x ETLs annealed at 220°C and 500°C.

	scan direction	PCE (%)	V_{OC} (V)	J_{SC} (mA cm^{-2})	FF (%)	HI (%)	R_s (Ω cm^2)	R_{sh} (Ω cm^2)	A	J_0 (mA cm^{-2})
220°C	reverse	15.70	1.14	20.95	65.7	15.3	3.54	1100	4.03	3.73×10^{-4}
(SnO_x)	forward	13.30	1.12	20.82	57.3					
500°C	reverse	13.17	1.02	20.64	62.9	22.5	3.90	650	4.15	1.56×10^{-3}
(HT-SnO_2)	forward	10.21	0.91	20.81	53.9					

200°C, and thus the residuals of the acetate could hinder the charge transfer and act as recombination sites. When the annealing temperature increased from 220°C to 500°C, J_{SC} changed slightly, whereas the open-circuit voltage (V_{OC}) and FF varied significantly and showed the same trend, first decreasing and then increasing. Thus, PSCs based on 300°C-annealed SnO_x showed the lowest PCE of 7.03%, which could be due to the phase transfer of the resulting SnO_x from amorphous to crystalline at 300°C [6]. The PCE then increased to 13.17% when the annealing temperature increased from 300°C to 500°C. Table 1 also demonstrates an important parameter, the hysteresis index (HI). This is used to describe the current–voltage hysteresis and is defined as $HI = (PCE|_{reverse} - PCE|_{forward})/PCE|_{reverse}$, where $PCE|_{reverse}$ and $PCE|_{forward}$ represent the PCE obtained from the reverse-scan and forward-scan J–V characteristics, respectively. PSCs with low-temperature (e.g. 220°C) annealed SnO_x ETLs exhibited suppressed hysteresis compared to those with high-temperature (e.g. 500°C) annealed SnO_2 ETLs.

The results presented above suggest that the low-temperature annealed SnO_x ETL outperformed its high-temperature counterpart, which are consistent with reported results [17,18]. We then conducted additional experiments and characterizations to reveal the origins of the improved performance of the low-temperature annealed SnO_x ETLs. For simplicity, further on we only discuss the results for the low-temperature (220°C) annealed SnO_x and the high-temperature (500°C) annealed SnO_2 (HT-SnO_2).

XPS measurements were conducted to investigate the chemical states of SnO_x and HT-SnO_2. As seen in figure 3*a*, SnO_x showed two characteristic peaks at 495.7 eV and 487.3 eV ($\Delta E = 8.4$ eV), which were assigned to Sn $3d_{3/2}$ and Sn $3d_{5/2}$, respectively. SnO_x also exhibited a peak at 931.2 eV in the O 1s XPS spectrum (figure 3*b*). These XPS results suggest that Sn was in the +4 valence state in SnO_x. There was no peak shift observed between SnO_x and HT-SnO_2 in Sn 3d and O 1s XPS spectra, which indicates that Sn was also in the +4 state in HT-SnO_2. Moreover, XAS measurements were performed to confirm the amorphous nature of SnO_x. In the Sn $M_{5,4}$-edge XAS spectra of HT-SnO_2 (figure 3*c*), two sets of triplet peaks (a, b, c) and (d, e, f) arose from $3d_{5/2}$ and $3d_{3/2}$ to 5p transitions, respectively. In figure 3*d*, peaks x and y corresponded to the hybridization of O 2p orbitals with Sn 5s and Sn 5p orbitals, respectively [35]. The Sn $M_{5,4}$-edge and O K-edge spectral features of HT-SnO_2 are consistent with the typical characteristics of crystalline SnO_2 in earlier reports [34,36,37]. For the SnO_x sample, significant differences were observed in the Sn $M_{5,4}$-edge spectral features. Peaks a and b broadened and merged into one peak h, and peaks d and e broadened and merged into i as well. This spectral broadening is related to the lack of long-range order in the structure of SnO_x and the

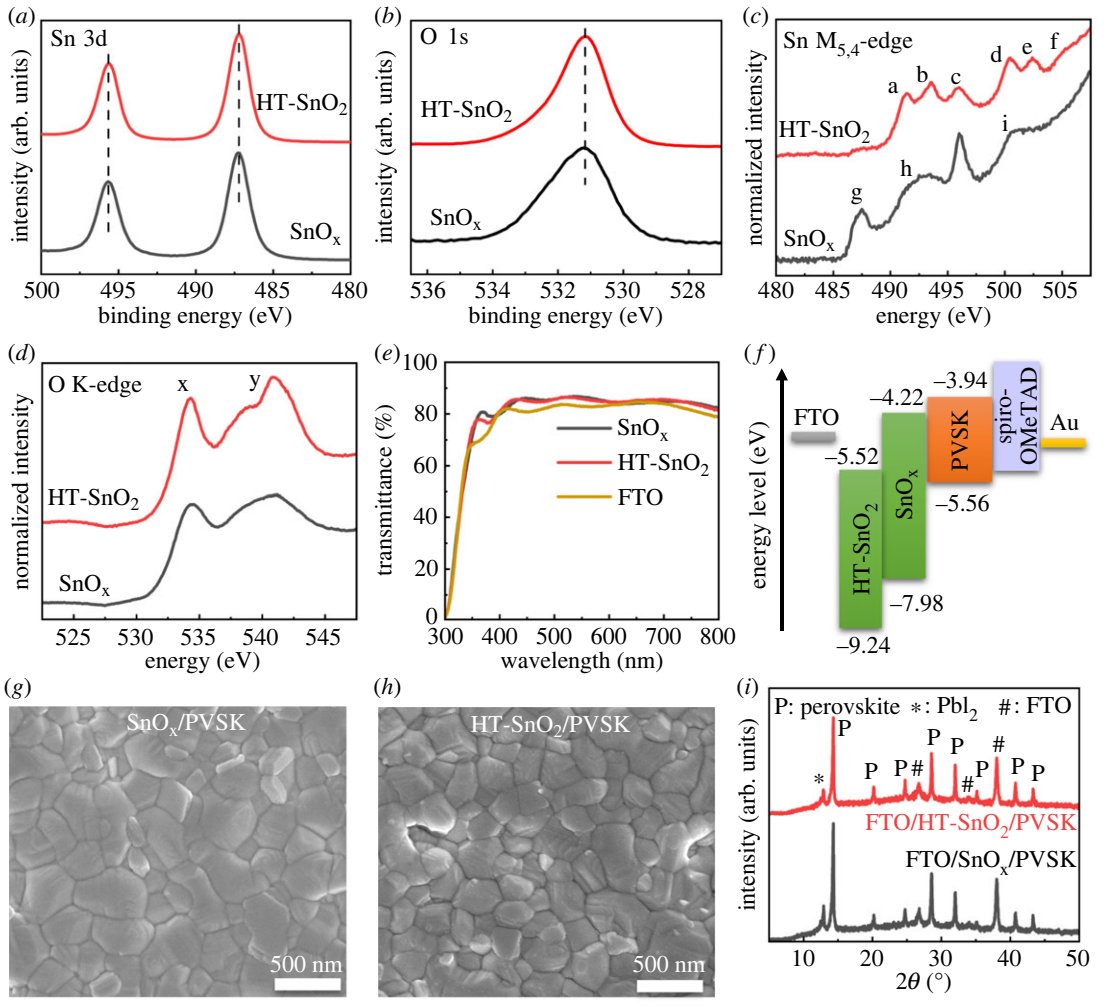

Figure 3. (*a*) Sn 3d XPS, (*b*) O 1s XPS, (*c*) Sn $M_{5,4}$-edge XAS, (*d*) O K-edge XAS, and (*e*) optical transmission spectra of SnO_x and HT-SnO_2; (*f*) energy level alignment of the PSC device with a SnO_x or HT-SnO_2 ETL; (*g*,*h*) SEM images and (*i*) XRD patterns of the perovskite films deposited on SnO_x and HT-SnO_2.

presence of uncoordinated surface tin atoms [38,39]. An additional pre-edge peak g appeared, which was assigned to the surface states originating from uncoordinated surface atoms, oxygen vacancies, or surface reconstruction [38–40]. As observed in the O K-edge spectrum of SnO_x, the spectral broadening was consistent with that in the Sn $M_{5,4}$-edge spectrum and was attributed to the presence of the surface states. These Sn $M_{5,4}$-edge and O K-edge spectral features of SnO_x are consistent with those of the amorphous SnO_x reported previously [37,41,42], confirming an amorphous structure without long-range order for the low-temperature annealed SnO_x.

The amorphous structure of SnO_x can be beneficial for the charge transport within ETLs. The grain boundary scattering within the nanocrystalline HT-SnO_2 could lead to electron transport losses, which would be less severe in the amorphous SnO_x [43,44]. This was verified by the improved conductivity of SnO_x (electronic supplementary material, figure S3). The conductivity of SnO_x was estimated to be 2.96×10^{-5} S cm^{-1}, which was slightly higher than that of HT-SnO_2 (2.46×10^{-5} S cm^{-1}). This enhanced conductivity can contribute to the improved J_{SC}. UV/Vis measurements were performed to examine the optical properties of SnO_x and HT-SnO_2 (figure 3*e*). SnO_x and HT-SnO_2 both showed an optical transmittance above 80% in the visible region (380–750 nm), which confirmed the transparency of the two samples. They also improved the optical transmission properties of FTO substrates because of the good antireflection ability of SnO_2 thin films [44,45]. Compared to HT-SnO_2, SnO_x exhibited a slightly enhanced transmittance, which could allow more light to reach the perovskite absorber to generate carriers, contributing to the enhanced J_{SC} of the devices based on SnO_x ETLs [45]. Furthermore, the optical band gap (E_g) can be determined by Tauc's relationship, which is described by $(\alpha h\nu)^2 = C \times (h\nu - E_g)$, where α is the optical absorption coefficient, $h\nu$ is the photon energy, and C

is a material constant [46]. The values of the band gap extrapolated from Tauc's plots (electronic supplementary material, figure S4) were 3.76 eV and 3.72 eV for SnO_x and HT-SnO_2, respectively. The enlarged band gap of SnO_x was consistent with the enhanced transmittance.

UPS measurements were performed to investigate the energy band levels of SnO_x and HT-SnO_2 (electronic supplementary material, figure S5*a*). The work function can be determined by the formula $E_F = 21.22 - (E_{onset} - E_{cutoff})$ [22], where E_F is the Fermi level, E_{onset} is the onset, and E_{cutoff} is the cutoff of the UPS spectrum. The work function of SnO_x and HT-SnO_2 was calculated to be 6.76 eV and 7.02 eV, respectively. The valence band maximum (E_{VBM}) of SnO_x and HT-SnO_2 was measured to be 1.22 eV and 2.22 eV below the Fermi level (electronic supplementary material, figure S5*b*), and then the E_{VBM} values were calculated to be −7.98 eV and −9.24 eV, respectively. Their conduction band minimums (E_{CBM}) were further determined to be −4.22 eV and −5.52 eV using the equation $E_{CBM} = E_{VBM} + E_g$. The energy band positions of the perovskite layer were obtained from the literature [47]. The energy band alignment diagram for PSCs based on SnO_x and HT-SnO_2 ETLs is shown in figure 3*f*. Compared to HT-SnO_2, SnO_x showed upshifted energy band levels and thus possessed an E_{CBM} much closer to that of the perovskite layer, enabling more efficient electron extraction and less V_{OC} losses at the SnO_x/perovskite interfaces. Moreover, the E_{CBM} of HT-SnO_2 was very close to the E_{VBM} of the perovskite layer, which could result in severe recombination of the electron–hole pairs at the HT-SnO_2/perovskite interfaces [48]. Therefore, SnO_x exhibited a better energy level alignment with the perovskite layer, thereby facilitating electron extraction and reducing recombination losses at the SnO_x/perovskite interfaces [49,50]. This could be the main reason why SnO_x ETLs offered improved V_{OC} and suppressed hysteresis compared with HT-SnO_2 ETLs.

The film morphology of the perovskite layers deposited on SnO_x and HT-SnO_2 was also investigated. As shown in the SEM images (figure 3*g*,*h*), the perovskite film deposited on SnO_x exhibited a larger average grain size of 293 nm than that of 242 nm for the perovskite film deposited on HT-SnO_2 (electronic supplementary material, figure S6). A few gaps appeared for the perovskite film deposited on HT-SnO_2. In the XRD patterns of the two perovskite films illustrated in figure 3*i*, three major peaks located at 14.3°, 28.6°, and 32.0° were assigned to (001), (002), and (012) crystal planes, respectively [51,52]. Compared to the HT-SnO_2/perovskite film, the SnO_x/perovskite film displayed increased relative intensity at both (001) and (002) peaks (electronic supplementary material, table S3), indicating enhanced crystallinity of the perovskite film with preferential growth along (001) and (002) planes [52,53]. Overall, the data showed that the SnO_x/perovskite film exhibited enlarged grains, improved morphology, and enhanced crystallinity. This might be attributed to the improved morphology of the amorphous SnO_x, thereby boosting the formation and crystallization of the perovskite film. The improved film quality of the perovskite layer can facilitate charge transport and reduce carrier recombination at grain boundaries, leading to enhanced device performance [54]. PL measurements were performed to investigate the charge transport kinetics at ETL/perovskite interfaces (electronic supplementary material, figure S7). The faster quenching indicated more efficient charge extraction and transport at the SnO_x/perovskite interface. Furthermore, the recombination characteristics of PSCs with SnO_x and HT-SnO_2 ETLs were obtained by fitting their J–V curves using an ideal diode mode: $J = J_{ph} - J_0 \times \exp[e(V + J \times R_s)/AKT]$ (electronic supplementary material, figure S8), where J_{ph} is the photo-induced current density, J_0 is the recombination current density, e is the elementary charge, R_s is the series resistance, A is the ideality factor, K is the Boltzmann constant, and T is the thermodynamic temperature [55]. The shunt resistance (R_{sh}) is calculated as $R_{sh} = -dV/dJ$ at $J = J_{SC}$. The values of these parameters are summarized in table 1. J_0 and the ideality factor both decreased, indicating suppressed charge recombination in the cells with SnO_x ETLs [45,55]. The reduced R_s and increased R_{sh} was also indicative of effective electron extraction and suppressed charge recombination at SnO_x/perovskite interfaces [43]. To summarize, the enhanced charge extraction and transport and suppressed charge recombination were ascribed to the enhanced electrical and optical properties of the amorphous SnO_x, improved film quality of the perovskite layer, and good energy level matching between the SnO_x ETL and the perovskite layer. Consequently, PSCs with SnO_x ETLs achieved improvements in all photovoltaic parameters (V_{OC}, J_{SC}, FF and PCE) and suppression of hysteresis compared to those with HT-SnO_2 ETLs.

The surface wettability of the substrates is crucial to film formation in the inkjet-printing deposition process, especially in a low-temperature solution process. Specifically, we fabricated three groups of PSCs using SnO_x ETLs printed on FTO substrates without surface treatment, with ultraviolet/ozone (UVO) treatment, and with pre-heating treatment. As shown in electronic supplementary material, figure S9 and table S4, the device performance was improved by applying either UVO or pre-heating treatment. Both UVO and pre-heating treatment can remove the organic residuals on the FTO substrates and

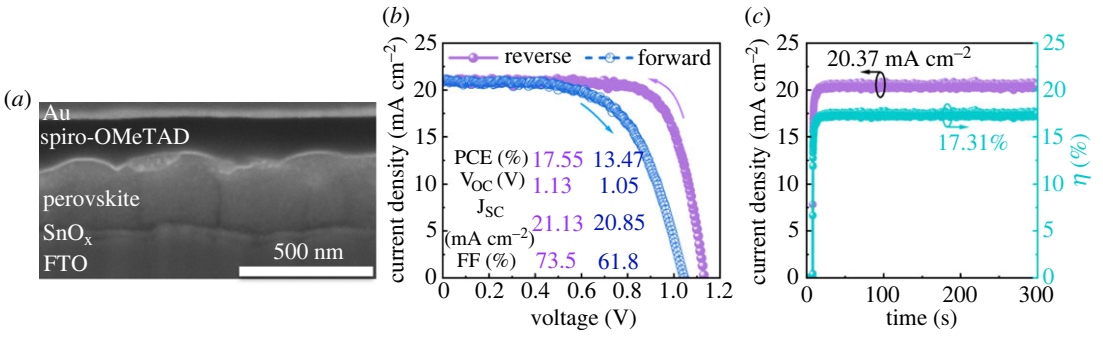

Figure 4. (*a*) Cross-sectional FIB/SEM image, (*b*) reverse-scan and forward-scan J–V curves, and (*c*) steady-state photocurrent density and stabilized efficiency (at a bias of 0.85 V) for the champion cell based on the inkjet-printed SnO_x ETL prepared from a 0.05 M precursor ink.

improve the wettability of the FTO substrates. This enabled the uniform deposition of SnO_x on the FTO substrates (electronic supplementary material, figure S9) and improved the interfacial contact between SnO_x and FTO, contributing to reduced recombination and thus improved performance with suppressed hysteresis [56,57]. Therefore, pre-heating treatment is a simple alternative to UVO cleaning in terms of substrate surface processing. We further optimized the performance of SnO_x-based devices by controlling the thickness of the SnO_x ETL, which was realized by adjusting the concentration of the precursor inks. As shown in figure 4*a* and electronic supplementary material, figure S10, the average thickness of the SnO_x ETL increased from 0 to 35 nm and 75 nm when the precursor concentration increased from 0 to 0.05 M and 0.1 M. Accordingly, the device performance varied with the thickness variation of the SnO_x ETL (electronic supplementary material, figure S11, figure S12, and table S5). The highest PCE of 17.55%, along with a forward-scan PCE of 13.47% (figure 4*b*), was obtained for the cell based on a SnO_x ETL with a thickness of approximately 35 nm. We also obtained a stabilized photocurrent density of 20.37 mA cm^{-2} and stabilized power output of 17.31% over 5 min (figure 4*c*). Moreover, PSCs with SnO_x ETLs exhibited improved performance with suppressed hysteresis compared with those without an ETL, regardless of the thickness of the SnO_x ETL. This proved that the inkjet-printed SnO_x as an ETL had the capability of separating charges, i.e. transporting electrons and blocking holes [17].

In comparable reports focused on inkjet-printed SnO_2 ETLs, Ghahremani *et al*. achieved a champion PCE of 13.08% [7], and Rohnacher *et al*. obtained a champion efficiency of 18.8% (12.0% in the forward scan) with a stabilized PCE of 15.2% over 5 min [6]. Our devices exhibited an improved stabilized efficiency and suppressed hysteresis compared to those in the latter report, although they did not deliver a PCE higher than 18.8%. Overall, we successfully fabricated solution-processed SnO_x ETLs as effective ETLs for planar PSCs by inkjet printing, which is expected to promote large-scale fabrication of PSCs.

3.2. Inkjet-printed solution-processed Cu : SnO_x electron transport layer ETL

Inkjet-printed solution-processed SnO_x has been established as an effective ETL for planar PSCs while there is still a motivation to further optimize this SnO_x ETL. The solution process used in the present work allows for doping SnO_x by adding a dopant precursor directly into the Sn precursor inks. Herein, we introduced Cu dopant into SnO_x ETLs and investigated the effects of Cu doping on the device performance. Various Cu : SnO_x ETLs were prepared from inks with different Cu concentrations of 2.5 at%, 5 at%, 7.5 at% and 10 at%. We then fabricated PSCs employing these Cu : SnO_x ETLs and obtained J–V characteristics of the devices (figure 5 and electronic supplementary material, figure S13). V_{OC} and FF decreased after Cu doping, while J_{SC} first increased and then decreased with increasing Cu doping level (electronic supplementary material, figure S14 and table S6). As a result, the devices with Cu : SnO_x ETLs produced lower PCEs than those with pristine SnO_x ETLs. Interestingly, the hysteresis index decreased dramatically from 16.2% to 1.5% when the Cu concentration increased from 0 to 2.5 at%. Afterwards, an inverted hysteresis phenomenon appeared, i.e. the PCE for the forward scan surpassed that for the reverse scan, when the Cu doping level further increased to 5 at% and higher levels. The inverted hysteresis mainly originated from the

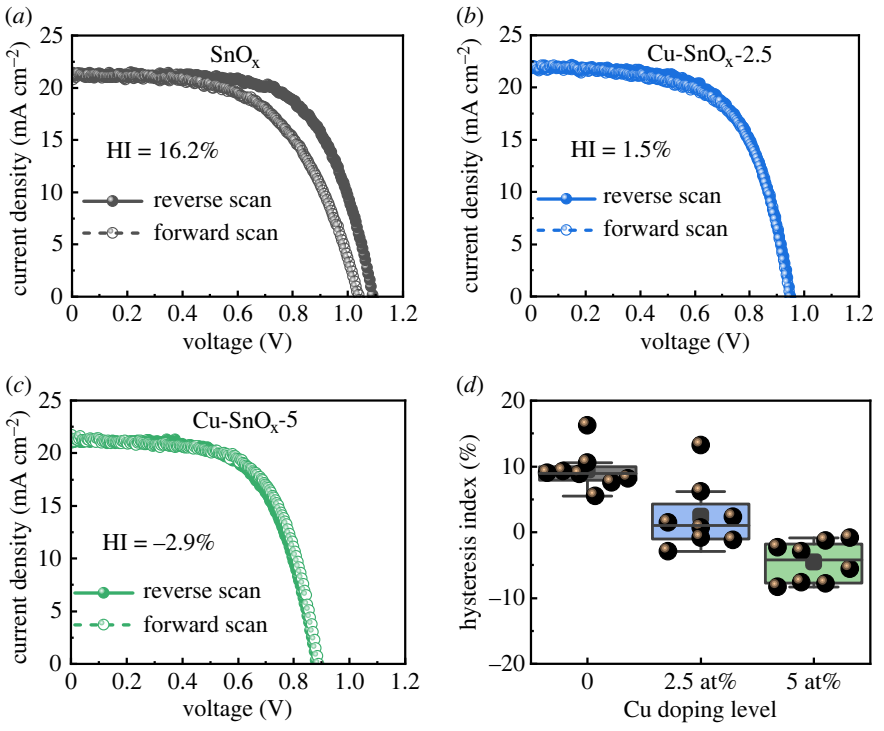

Figure 5. Reverse-scan and forward-scan J–V characteristics of PSCs based on (*a*) pristine SnO_x, (*b*) 2.5 at% Cu : SnO_x, and (*c*) 5 at% Cu : SnO_x; (*d*) distribution of the hysteresis index for PSCs based on pristine SnO_x and Cu : SnO_x ETLs.

improved FF for the forward scan compared to that for the reverse scan (electronic supplementary material, figure S14). In addition, we fabricated PSCs using 500°C-annealed Cu : SnO_x ETLs. The devices exhibited reduced performance compared to those with 220°C-annealed counterparts (electronic supplementary material, figure S15). This result is consistent with that for the undoped SnO_x.

To reveal the origin of the effects of Cu doping on the device performance, various characterizations and measurements were conducted. The XRD patterns in electronic supplementary material, figure S16, show that no crystalline peaks were observed for Cu : SnO_x. All the Cu : SnO_x thin films exhibited dense and compact surfaces with no pinholes (electronic supplementary material, figure S17). The SEM images also imply that Cu doping did not have a significant influence on the film morphology. From figure 6*a* and electronic supplementary material, figure S18, the peaks of the O 1s and Sn 3d XPS spectra shifted to lower binding energies upon Cu doping, indicating a strong chemical interaction between Cu and SnO_x [26]. As seen in figure 6*b*, the Cu 2p peaks were detected for 5 at% Cu : SnO_x while the signal was very weak for 2.5 at% Cu : SnO_x. The energy peak at 932.2 eV indicated the presence of Cu^+ oxidation state, and the observable satellite features at 942.3 eV represented the +2 state of Cu [30]. Therefore, there were two oxidation states of Cu^+ and Cu^{2+} in Cu : SnO_x. Moreover, both Sn $M_{5,4}$-edge and O K-edge XAS spectra only exhibited intensity variations in the characteristic peaks upon Cu doping (electronic supplementary material, figure S19). The XPS and XAS results suggested that SnO_x was successfully doped with Cu. As shown in figure 6*a*, the O 1s XPS peak of SnO_x can be deconvoluted into two peaks. The peak at 531.2 eV originated from lattice oxygen (O_L) and the other peak at 532.6 eV was assigned to oxygen vacancies or adsorbed hydroxyl groups (O_V) [58,59]. The peak ratio of O_V to total oxygen increased from 24.11% to 30.92% when the Cu doping concentration increased from 0 to 2.5 at%, and then significantly increased to 52.53% when the Cu doping level increased to 5 at% (electronic supplementary material, table S7). These surface oxygen defects (oxygen vacancies or hydroxyl groups) could cause carrier recombination and poor charge transfer for PSCs [30,60,61].

The surface chemistry of ETLs can influence the formation and crystallinity of the perovskite layers [30]. For the perovskite film deposited on Cu-doped SnO_x compared to that deposited on SnO_x (electronic supplementary material, figure S20, and figure 3*g*), the average crystal grain size decreased, and a few white PbI_2 spots appeared. This was confirmed by the XRD patterns (electronic supplementary material, figure S21), in which the intensity ratio of the peak at 14.3° for perovskite to the peak at 12.9° for PbI_2 decreased upon Cu doping (electronic supplementary material, table S8).

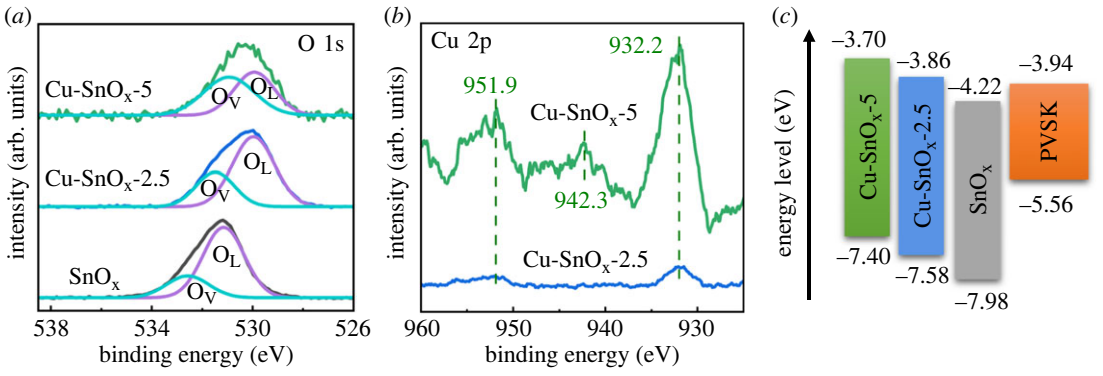

Figure 6. (*a*) O 1s and (*b*) Cu 2p XPS spectra for pristine, 2.5 at%, and 5 at% Cu-doped SnO_x; (*c*) energy level alignment of the pristine, 2.5 at%, and 5 at% Cu-doped SnO_x ETL with the perovskite layer.

Thus, Cu-doped SnO_x exerted a negative effect on the film quality of the perovskite layers, resulting in recombination losses and poor charge transport. This effect was further investigated by PL measurements of the perovskite layers (electronic supplementary material, figure S22). The higher PL intensity represented more severe charge recombination and worse charge transport ability at the Cu-doped SnO_x/perovskite interfaces [26,31]. The Cu-SnO_x-5/perovskite film exhibited a much higher PL intensity than the Cu-SnO_x-2.5/perovskite film, which might be mainly attributed to the presence of a substantial number of oxygen defects on the surface of the 5 at% Cu-doped SnO_x. Consequently, PSCs based on Cu-doped SnO_x ETLs suffered from degradation in device performance (V_{OC}, FF, and PCE). With a few exceptions, the devices with 2.5 at% Cu-doped SnO_x offered an enhanced J_{SC} compared to those with pristine SnO_x, which was attributed to the improved conductivity (electronic supplementary material, figure S23) [25].

The optical transmittance of the Cu-doped samples decreased slightly compared to that of the pristine SnO_x (electronic supplementary material, figure S24*a*). Then, the values of the optical band gap extracted from Tauc's plots (electronic supplementary material, figure S24*b*) were 3.72 eV and 3.70 eV for 2.5 at% and 5 at% Cu-doped SnO_x, respectively. The reduced band gap could originate from the increased surface defect states upon Cu doping [62]. Furthermore, the energy band positions of Cu-doped SnO_x were obtained from the UPS and valence band XPS measurements (electronic supplementary material, figure S25 and table S9). As shown in figure 6*c*, the conduction band minimum of the two Cu-doped SnO_x ETLs was significantly upshifted to become shallower than that of the perovskite layer, which could form unfavourable electron extraction barriers and thus cause charge/ion accumulation at the ETL/perovskite interface [63]. The conduction band offset between Cu-doped SnO_x and perovskite increased when the Cu doping level increased from 2.5 at% to 5 at%, leading to increased charge/ion accumulation at the ETL/perovskite interface [64,65]. This could account for the increase in HI (absolute value). The decrease in HI from 0 to 2.5 at% was probably due to the enhanced conductivity which might alleviate the hysteresis by balancing the electron flux and hole flux with PSCs [25,66].

The origin of normal hysteresis has been attributed to ion migration and accumulation at interfaces, which screens the electric field and leads to a decrease in V_{OC} and FF in the forward scan [67–69]. According to a previous study [70], in the case of extraction barriers, these accumulated ionic charges also formed dipole layers with piled-up electronic charges at the ETL/perovskite interface, which enhanced the electric field and improved the FF for the forward scan, resulting in an inverted hysteresis. Therefore, the observed inverted hysteresis in our devices was related to the charge/ion accumulation induced by the energetic extraction barriers at Cu-doped SnO_x/perovskite interfaces. Besides, the relatively low scan rate (125 mV s^{-1}) used in this work also allowed the occurrence of a slow ion migration process, thus intensifying the impact of extraction barriers on charge extraction, leading to an inverted hysteresis [65,70]. Furthermore, the hysteretic behaviour transferred from normal hysteresis to inverted hysteresis when the Cu doping level increased from 2.5 at% to 5 at%, although there were energy barriers at both Cu-doped SnO_x/perovskite interfaces. A similar phenomenon was reported by Rong *et al.*, who achieved tunable hysteresis for carbon-based PSCs by adjusting the thickness of a compact TiO_2 ETL [71]. They ascribed the origin of this phenomenon to the interplay between the slow dynamics of charge accumulation and changes in recombination rates. In our work, in addition to the changes in charge/ion accumulation induced by the enlarged

conduction band offset, the recombination losses at the ETL/perovskite interfaces also varied, originating from variations in the quantity of oxygen defects on the Cu-doped SnO_x surfaces and defects on the perovskite films with increasing Cu content. Therefore, the transformation of hysteresis from normal to inverted can be attributed to the interplay between charge/ion accumulation and recombination at the Cu-doped SnO_x/perovskite interfaces. The exact origin of this phenomenon is still under investigation.

Our results regarding the effect of Cu doping were quite different from those reported in the literature [30,31], in which Cu-doped SnO_2 based PSCs exhibited an improved PCE with normal hysteresis. The disparity in the device performance could originate from the differences in the morphological, structural, electronic, and optical properties between our Cu-doped SnO_x and their Cu-doped SnO_2. Our results imply that elemental doping does not always lead to a favourable performance improvement. The selection of the doping element and the concentration of the selected dopant are of great importance in determining the PSC device performance. This work demonstrates a method for tuning the hysteresis of SnO_x-based PSCs through Cu doping. An acceptable PCE of 13.15% with a low hysteresis of 1.5% was obtained for the device with a 2.5 at% Cu-doped SnO_x ETL. However, further investigations including stability measurements are required to verify the advantages of this low hysteresis.

4. Conclusion

In summary, we have successfully fabricated solution-processed inkjet-printed SnO_x as effective ETLs for planar PSCs. The effect of the annealing temperature of the SnO_x ETL on the device performance was studied. The low-temperature annealed amorphous SnO_x ETLs outperformed their high-temperature annealed crystalline counterparts. The improved device performance originated from enhanced charge extraction and transport and suppressed charge recombination at ETL/perovskite interfaces, which was attributed to the enhanced electrical and optical properties of the amorphous SnO_x, improved film quality of the perovskite layer, and better energy level alignment between the SnO_x ETL and perovskite layer. Through further optimization of the substrate surface treatment and the film thickness of the SnO_x ETL, a champion efficiency of 17.55% was achieved. Thereafter, Cu was incorporated into SnO_x. Upon Cu doping, SnO_x showed increased surface defects and upshifted energy levels, and the perovskite film also exhibited increased defects, resulting in the reduction in the device performance. Moreover, the devices with Cu-doped SnO_x ETLs exhibited tunable hysteresis, which was suppressed and then transformed into an inverted hysteresis with increasing Cu doping concentration. The reduced hysteresis for the 2.5 at% Cu-doped SnO_x ETLs was probably due to the enhanced conductivity. The inverted hysteresis was related to the energetic extraction barriers at Cu-doped SnO_x/perovskite interfaces. Therefore, the transformation of hysteresis from normal to inverted can be attributed to the interplay between charge/ion accumulation and recombination at Cu-doped SnO_x/perovskite interfaces in the case of extraction barriers. This work provides an approach to fabricate ETLs in a sustainable and scalable manner and a platform for the fabrication of fully inkjet-printed PSCs in future work.

Ethics. This work did not require ethical approval from a human subject or animal welfare committee.

Data accessibility. The datasets supporting this article have been uploaded as part of the electronic supplementary material [72].

Declaration of AI use. We have not used AI-assisted technologies in creating this article.

Authors' contributions. D.L.: conceptualization, data curation, formal analysis, funding acquisition, investigation, methodology, project administration, visualization, writing—original draft, writing—review and editing; F.Y.: investigation; C.D.: investigation, writing—review and editing; J.G.: resources, supervision, writing—review and editing; J.J.U.: resources; L.B.: conceptualization, funding acquisition, investigation, methodology, project administration, resources, supervision, writing—review and editing.

All authors gave final approval for publication and agreed to be held accountable for the work performed therein.

Conflict of interest declaration. We declare we have no competing interests.

Funding. This research was funded by China Scholarship Council and Jernkontoret (Stiftelsen Jernkontorsfonden för Bergsvetenskaplig Forskning). This research used resources of the Advanced Light Source, which is a DOE Office of Science User Facility under Contract no. DE-AC02-05CH11231. Work at the Molecular Foundry was supported by the Office of Science, Office of Basic Energy Sciences, of the US Department of Energy under Contract no. DE-AC02-05CH11231.

Acknowledgments. Prof. James M. Gardner and Dr Mahboubeh Jamshidi are sincerely acknowledged for their help with some of the characterizations.

References

1. National Renewable Energy Laboratory. 2023 Best research-cell efficiencies. See https://www.nrel.gov/pv/interactive-cell-efficiency.html (accessed 29 June 2023).
2. Hopkinson N, Smith PJ. 2017 Industrial 3D inkjet printing/additive manufacturing. In *Handbook of industrial inkjet printing* (ed. W Zapka), pp. 649–660. Weinheim, Germany: Wiley-VCH.
3. Schackmar F, Eggers H, Frericks M, Richards BS, Lemmer U, Hernandez-Sosa G, Paetzold UW. 2021 Perovskite solar cells with all-inkjet-printed absorber and charge transport layers. *Adv. Mater. Technol.* **6**, 2000271. (doi:10.1002/admt.202000271)
4. Eggers H, Schackmar F, Abzieher T, Sun Q, Lemmer U, Vaynzof Y, Richards BS, Hernandez-Sosa G, Paetzold UW. 2020 Inkjet-printed micrometer-thick perovskite solar cells with large columnar grains. *Adv. Energy Mater.* **10**, 1903184. (doi:10.1002/aenm.201903184)
5. Gheno A, Huang Y, Bouclé J, Ratier B, Rolland A, Even J, Vedraine S. 2018 Toward highly efficient inkjet-printed perovskite solar cells fully processed under ambient conditions and at low temperature. *Sol. RRL* **2**, 1800191. (doi:10.1002/solr.201800191)
6. Rohnacher V *et al.* 2021 Analytical study of solution-processed tin oxide as electron transport layer in printed perovskite solar cells. *Adv. Mater. Technol.* **6**, 2000282. (doi:10.1002/admt.202000282)
7. Ghahremani AH, Ratnayake D, Sherehiy A, Popa DO, Druffel T. 2021 Automated fabrication of perovskite photovoltaics using inkjet printing and intense pulse light annealing. *Energy Technol.* **9**, 2100452. (doi:10.1002/ente.202100452)
8. Lu D, Zhang W, Kloo L, Belova L. 2021 Inkjet-printed electron transport layers for perovskite solar cells. *Materials* **14**, 7525. (doi:10.3390/ma14247525)
9. Zhang T, He Q, Yu J, Chen A, Zhang Z, Pan J. 2022 Recent progress in improving strategies of inorganic electron transport layers for perovskite solar cells. *Nano Energy* **104**, 107918. (doi:10.1016/j.nanoen.2022.107918)
10. Lu H, Tian W, Gu B, Zhu Y, Li L. 2017 TiO_2 electron transport bilayer for highly efficient planar perovskite solar cell. *Small* **13**, 1701535. (doi:10.1002/smll.201701535)
11. Zhou J *et al.* 2022 SnO_2 quantum dot-modified mesoporous TiO_2 electron transport layer for efficient and stable perovskite solar cells. *ACS Appl. Energy Mater.* **5**, 3052–3063. (doi:10.1021/acsaem.1c03681)
12. Jiang Q *et al.* 2016 Enhanced electron extraction using SnO_2 for high-efficiency planar-structure $HC(NH_2)_2PbI_3$-based perovskite solar cells. *Nat. Energy* **2**, 16177. (doi:10.1038/nenergy.2016.177)
13. Deng K, Chen Q, Li L. 2020 Modification engineering in SnO_2 electron transport layer toward perovskite solar cells: efficiency and stability. *Adv. Funct. Mater.* **30**, 2004209. (doi:10.1002/adfm.202004209)
14. Ke W *et al.* 2015 Low-temperature solution-processed tin oxide as an alternative electron transporting layer for efficient perovskite solar cells. *J. Am. Chem. Soc.* **137**, 6730–6733. (doi:10.1021/jacs.5b01994)
15. Blackburn D, Routledge T, O'kane M, Cassella EJ, Game OS, Catley TE, Wood CJ, Mcardle T, Lidzey DG. 2022 Low-temperature, scalable, reactive deposition of tin oxide for perovskite solar cells. *Sol. RRL* **6**, 2200263. (doi:10.1002/solr.202200263)
16. Cheng N, Yu Z, Li W, Lei B, Zi W, Xiao Z, Zhao Z, Zong P-A. 2022 Low temperature processed SnO_2 electron transporting layer from tin oxalate for perovskite solar cells. *ACS Appl. Energy Mater.* **5**, 15 385–15 391. (doi:10.1021/acsaem.2c03002)
17. Jung K-H, Seo J-Y, Lee S, Shin H, Park N-G. 2017 Solution-processed SnO_2 thin film for a hysteresis-free planar perovskite solar cell with a power conversion efficiency of 19.2%. *J. Mater. Chem. A* **5**, 24 790–24 803. (doi:10.1039/C7TA08040A)
18. Ke W, Zhao D, Cimaroli AJ, Grice CR, Qin P, Liu Q, Xiong L, Yan Y, Fang G. 2015 Effects of annealing temperature of tin oxide electron selective layers on the performance of perovskite solar cells. *J. Mater. Chem. A* **3**, 24 163–24 168. (doi:10.1039/C5TA06574G)
19. Zhong JX *et al.* 2022 Room temperature fabrication of SnO_2 electrodes enabling barrier-free electron extraction for efficient flexible perovskite photovoltaics. *Adv. Funct. Mater.* **32**, 2200817. (doi:10.1002/adfm.202200817)
20. Xing Y *et al.* 2022 LiF-modified SnO_2 electron transport layer improves the performance of carbon-based all-inorganic $CsPbIBr_2$ perovskite solar cells. *Energy Fuels* **36**, 13 179–13 186. (doi:10.1021/acs.energyfuels.2c02797)
21. Wang L *et al.* 2022 Robust interfacial modifier for efficient perovskite solar cells: reconstruction of energy alignment at buried interface by self-diffusion of dopants. *Adv. Funct. Mater.* **32**, 2204725. (doi:10.1002/adfm.202204725)
22. Wang J, Wang Z, Chen S, Jiang N, Yuan L, Zhang J, Duan Y. 2022 Reduced surface hydroxyl and released interfacial strain by inserting CsF anchor interlayer for high-performance perovskite solar cells. *Sol. RRL* **7**, 2200960. (doi:10.1002/solr.202200960)
23. Liu C, Guo M, Su H, Zhai P, Xie K, Liu Z, Zhang J, Liu L, Fu H. 2022 Highly improved efficiency and stability of planar perovskite solar cells via bifunctional phytic acid dipotassium anchored SnO_2 electron transport layer. *Appl. Surf. Sci.* **588**, 152943. (doi:10.1016/j.apsusc.2022.152943)
24. Song J, Zhang W, Wang D, Deng K, Wu J, Lan Z. 2019 Colloidal synthesis of Y-doped SnO_2 nanocrystals for efficient and slight hysteresis planar perovskite solar cells. *Sol. Energy* **185**, 508–515. (doi:10.1016/j.solener.2019.04.084)
25. Park M, Kim J-Y, Son HJ, Lee C-H, Jang SS, Ko MJ. 2016 Low-temperature solution-processed Li-doped SnO_2 as an effective electron transporting layer for high-performance flexible and wearable perovskite solar cells. *Nano Energy* **26**, 208–215. (doi:10.1016/j.nanoen.2016.04.060)
26. Wang R, Wu J, Wei S, Zhu J, Guo M, Zheng Q, Wei M, Cheng S. 2022 Gadolinium-doped SnO_2 electron transfer layer for highly efficient planar perovskite solar cells. *J. Power Sources* **544**, 231870. (doi:10.1016/j.jpowsour.2022.231870)
27. Halvani Anaraki E *et al.* 2018 Low-temperature Nb-doped SnO_2 electron-selective contact yields over 20% efficiency in planar perovskite solar cells. *ACS Energy Lett.* **3**, 773–778. (doi:10.1021/acsenergylett.8b00055)
28. Ye H, Liu Z, Liu X, Sun B, Tan X, Tu Y, Shi T, Tang Z, Liao G. 2019 17.78% efficient low-temperature carbon-based planar perovskite solar cells using Zn-doped SnO_2 electron transport layer. *Appl. Surf. Sci.* **478**, 417–425. (doi:10.1016/j.apsusc.2019.01.237)
29. Kim J, Murdoch BJ, Partridge JG, Xing K, Qi D-C, Lipton-Duffin J, Mcconville CF, Van Embden J, Gaspera ED. 2020 Ultrasonic spray pyrolysis of antimony-doped tin oxide transparent conductive coatings. *Adv. Mater. Interfaces* **7**, 2000655. (doi:10.1002/admi.202000655)
30. Zhou X *et al.* 2022 Solution-processed Cu-doped SnO_2 as an effective electron transporting layer for high-performance planar perovskite solar cells. *Appl. Surf. Sci.* **584**, 152651. (doi:10.1016/j.apsusc.2022.152651)
31. Bahadur J, Ghahremani AH, Martin B, Pishgar S, Sunkara MK, Druffel T, Pal K. 2022 Solution-processed Cu:SnO_2 as an efficient electron transport layer for fabrication of low-temperature planar perovskite solar cell under ambient conditions. *IEEE J. Photovoltaics* **12**, 1162–1169. (doi:10.1109/JPHOTOV.2022.3162340)
32. Fang M. 2012 Properties of multifunctional oxide thin films deposited by ink-jet printing. Doctoral thesis, KTH Royal Institute of Technology, Stockholm, Sweden.
33. Chen C *et al.* 2017 Cu(II) complexes as p-type dopants in efficient perovskite solar cells. *ACS Energy Lett.* **2**, 497–503. (doi:10.1021/acsenergylett.6b00691)
34. Bae J-Y, Park J, Kim HY, Kim H-S, Park J-S. 2015 Facile route to the controlled synthesis of tetragonal and orthorhombic SnO_2 films by mist chemical vapor deposition. *ACS Appl. Mater. Interfaces* **7**, 12 074–12 079. (doi:10.1021/acsami.5b02251)
35. Minohara M, Kikuchi N, Yoshida Y, Kumigashira H, Aiura Y. 2019 Improvement of the hole mobility of SnO epitaxial films grown by pulsed laser deposition. *J. Mater. Chem. C* **7**, 6332–6336. (doi:10.1039/C9TC01297D)
36. Wang D, Yang J, Li X, Wang J, Li R, Cai M, Sham TK, Sun X. 2012 Observation of surface/defect states of SnO_2 nanowires on different substrates from X-ray excited optical luminescence. *Cryst. Growth Des.* **12**, 397–402. (doi:10.1021/cg2011919)
37. Haeberle J, Machulik S, Janowitz C, Manzke R, Gaspar D, Barquinha P, Schmeißer D. 2016 Gap states in the electronic structure of SnO_2 single

crystals and amorphous SnO_x thin films. *J. Appl. Phys.* **120**, 105101. (doi:10.1063/1.4962313)
38. Jaiswal MK, Kumar R, Kanjilal D, Dong CL, Chen CL, Asokan K, Ojha S. 2015 Studies of dense electronic excitation-induced modification in crystalline Fe-doped SnO_2 thin films. *Appl. Surf. Sci.* **332**, 726–735. (doi:10.1016/j.apsusc.2014.12.182)
39. Kucheyev SO, Baumann TF, Sterne PA, Wang YM, Van Buuren T, Hamza AV, Terminello LJ, Willey TM. 2005 Surface electronic states in three-dimensional SnO_2 nanostructures. *Phys. Rev. B* **72**, 035404. (doi:10.1103/PhysRevB.72.035404)
40. Baumann TF, Kucheyev SO, Gash AE, Satcher Jr JH. 2005 Facile synthesis of a crystalline, high-surface-area SnO_2 aerogel. *Adv. Mater.* **17**, 1546–1548. (doi:10.1002/adma.200500074)
41. Sharma V, Vyas R, Bazylewski P, Chang GS, Asokan K, Sachdev K. 2016 Probing the highly transparent and conducting SnOx/Au/SnOx structure for futuristic TCO applications. *RSC Adv.* **6**, 29 135–29 141. (doi:10.1039/C5RA24422F)
42. Nesov SN, Bolotov VV, Korusenko PM, Povoroznyuk SN, Vilkov OY. 2016 Interfacial interaction in a composite based on multi-walled carbon nanotubes and amorphous tin oxide. *Phys. Solid State* **58**, 997–1003. (doi:10.1134/S1063783416050164)
43. Zhang X *et al.* 2022 Amorphous TiO_2 film with fiber like structure: an ideal candidate for ETL of perovskite solar cells. *Mater. Lett.* **324**, 132684. (doi:10.1016/j.matlet.2022.132684)
44. Zhang L *et al.* 2023 Amorphous F-doped TiO_x caulked SnO_2 electron transport layer for flexible perovskite solar cells with efficiency exceeding 22.5%. *Adv. Funct. Mater.* **33**, 2213961. (doi:10.1002/adfm.202213961)
45. Yang G *et al.* 2017 Reducing hysteresis and enhancing performance of perovskite solar cells using low-temperature processed Y-doped SnO_2 nanosheets as electron selective layers. *Small* **13**, 1601769. (doi:10.1002/smll.201601769)
46. Tauc J, Menth A. 1972 States in the gap. *J. Non-Cryst. Solids* **8**, 569–585. (doi:10.1016/0022-3093(72)90194-9)
47. Song S, Kang G, Pyeon L, Lim C, Lee G-Y, Park T, Choi J. 2017 Systematically optimized bilayered electron transport layer for highly efficient planar perovskite solar cells ($\eta = 21.1\%$). *ACS Energy Lett.* **2**, 2667–2673. (doi:10.1021/acsenergylett.7b00888)
48. Huang X, Hu Z, Xu J, Wang P, Wang L, Zhang J, Zhu Y. 2017 Low-temperature processed SnO_2 compact layer by incorporating TiO_2 layer toward efficient planar heterojunction perovskite solar cells. *Sol. Energy Mater. Sol. Cells* **164**, 87–92. (doi:10.1016/j.solmat.2017.02.010)
49. Noh YW, Lee JH, Jin IS, Park SH, Jung JW. 2019 Tailored electronic properties of Zr-doped SnO_2 nanoparticles for efficient planar perovskite solar cells with marginal hysteresis. *Nano Energy* **65**, 104014. (doi:10.1016/j.nanoen.2019.104014)
50. Wang P *et al.* 2021 Cobalt chloride hexahydrate assisted in reducing energy loss in perovskite solar cells with record open-circuit voltage of 1.20 V. *ACS Energy Lett.* **6**, 2121–2128. (doi:10.1021/acsenergylett.1c00443)
51. Jeon NJ, Noh JH, Yang WS, Kim YC, Ryu S, Seo J, Seok SI. 2015 Compositional engineering of perovskite materials for high-performance solar cells. *Nature* **517**, 476–480. (doi:10.1038/nature14133)
52. Xu Z *et al.* 2019 A thermodynamically favored crystal orientation in mixed formamidinium/methylammonium perovskite for efficient solar cells. *Adv. Mater.* **31**, 1900390. (doi:10.1002/adma.201900390)
53. Alexander A, Kamalon VP, Dev VV, Raees AM, Reghunathan S, Nair PR, Namboothiry MAG. 2023 Enhancing the efficiency and stability of perovskite solar cells through defect passivation and controlled crystal growth using allantoin. *ACS Appl. Mater. Interfaces* **15**, 58 406–58 415. (doi:10.1021/acsami.3c13591)
54. Song Z, Xu W, Wu Y, Liu S, Bi W, Chen X, Song H. 2020 Incorporating of lanthanide ions into perovskite film for efficient and stable perovskite solar cells. *Small* **16**, 2001770. (doi:10.1002/smll.202001770)
55. Dong J, Shi J, Li D, Luo Y, Meng Q. 2015 Controlling the conduction band offset for highly efficient ZnO nanorods based perovskite solar cell. *Appl. Phys. Lett.* **107**, 073507. (doi:10.1063/1.4929435)
56. Ke W *et al.* 2015 Efficient hole-blocking layer-free planar halide perovskite thin-film solar cells. *Nat. Commun.* **6**, 6700. (doi:10.1038/ncomms7700)
57. Méndez PF, Muhammed SKM, Barea EM, Masi S, Mora-Seró I. 2019 Analysis of the UV–ozone-treated SnO_2 electron transporting layer in planar perovskite solar cells for hHigh performance and reduced hysteresis. *Sol. RRL* **3**, 1900191. (doi:10.1002/solr.201900191)
58. Yi Z, Xiao B, Li X, Luo Y, Jiang Q, Yang J. 2023 Novel dual-modification strategy using Ce-containing compounds toward high-performance flexible perovskite solar cells. *Nano Energy* **109**, 108241. (doi:10.1016/j.nanoen.2023.108241)
59. Gao F *et al.* 2023 Porous organic cage induced spontaneous restructuring of buried interface toward high-performance perovskite photovoltaic. *Adv. Funct. Mater.* **33**, 2211900. (doi:10.1002/adfm.202211900)
60. Mohamad Noh MF, Arzaee NA, Safaei J, Mohamed NA, Kim HP, Mohd Yusoff AR, Jang J, Mat Teridi MA. 2019 Eliminating oxygen vacancies in SnO_2 films via aerosol-assisted chemical vapour deposition for perovskite solar cells and photoelectrochemical cells. *J. Alloys Compd.* **773**, 997–1008. (doi:10.1016/j.jallcom.2018.09.273)
61. Bai G *et al.* 2019 High performance perovskite sub-module with sputtered SnO_2 electron transport layer. *Sol. Energy* **183**, 306–314. (doi:10.1016/j.solener.2019.03.026)
62. Babu B, Kadam AN, Ravikumar RVSSN, Byon C. 2017 Enhanced visible light photocatalytic activity of Cu-doped SnO_2 quantum dots by solution combustion synthesis. *J. Alloys Compd.* **703**, 330–336. (doi:10.1016/j.jallcom.2017.01.311)
63. Correa Baena JP *et al.* 2015 Highly efficient planar perovskite solar cells through band alignment engineering. *Energy Environ. Sci.* **8**, 2928–2934. (doi:10.1039/C5EE02608C)
64. García-Rosell M, Bou A, Jiménez-Tejada JA, Bisquert J, Lopez-Varo P. 2018 Analysis of the influence of selective contact heterojunctions on the performance of perovskite solar cells. *J. Phys. Chem. C* **122**, 13 920–13 925. (doi:10.1021/acs.jpcc.8b01070)
65. Pham ND *et al.* 2019 Tailoring crystal structure of $FA_{0.83}Cs_{0.17}PbI_3$ perovskite through guanidinium doping for enhanced performance and tunable hysteresis of planar perovskite solar cells. *Adv. Funct. Mater.* **29**, 1806479. (doi:10.1002/adfm.201806479)
66. Heo JH, Han HJ, Kim D, Ahn TK, Im SH. 2015 Hysteresis-less inverted $CH_3NH_3PbI_3$ planar perovskite hybrid solar cells with 18.1% power conversion efficiency. *Energy Environ. Sci.* **8**, 1602–1608. (doi:10.1039/C5EE00120J)
67. Tress W, Marinova N, Moehl T, Zakeeruddin SM, Nazeeruddin MK, Grätzel M. 2015 Understanding the rate-dependent J–V hysteresis, slow time component, and aging in $CH_3NH_3PbI_3$ perovskite solar cells: the role of a compensated electric field. *Energy Environ. Sci.* **8**, 995–1004. (doi:10.1039/C4EE03664F)
68. Chen B *et al.* 2015 Impact of capacitive effect and ion migration on the hysteretic behavior of perovskite solar cells. *J. Phys. Chem. Lett.* **6**, 4693–4700. (doi:10.1021/acs.jpclett.5b02229)
69. Li C, Tscheuschner S, Paulus F, Hopkinson PE, Kießling J, Köhler A, Vaynzof Y, Huettner S. 2016 Iodine migration and its effect on hysteresis in perovskite solar cells. *Adv. Mater.* **28**, 2446–2454. (doi:10.1002/adma.201503832)
70. Tress W, Correa Baena JP, Saliba M, Abate A, Graetzel M. 2016 Inverted current–voltage hysteresis in mixed perovskite solar cells: polarization, energy barriers, and defect recombination. *Adv. Energy Mater.* **6**, 1600396. (doi:10.1002/aenm.201600396)
71. Rong Y *et al.* 2017 Tunable hysteresis effect for perovskite solar cells. *Energy Environ. Sci.* **10**, 2383–2391. (doi:10.1039/C7EE02048A)
72. Lu D, Yang F, Dun C, Guo J, Urban JJ, Belova L. 2024 Inkjet-printed SnO_x as an effective electron transport layer for planar perovskite solar cells and the effect of Cu doping. Figshare. (doi:10.6084/m9.figshare.c.7074851)